PCCP

ROYAL SOCIETY OF CHEMISTRY

PAPER

View Article Online
View Journal | View Issue

Check for updates

Cite this: *Phys. Chem. Chem. Phys.*, 2026, **28**, 4806

Received 3rd November 2025,
Accepted 13th January 2026

DOI: 10.1039/d5cp04239a

rsc.li/pccp

First-principles insights into chromium-induced oxide phases in NiO

Xiao Peng,[ab] Jianmin Chen,[ab] Xin Yan,[ab] Wentao Wu,[c] Wang Zhu,[ab] Canying Cai,*[ab] Yujing Liu*[d] and Guangwen Zhou *[e]

The high-temperature oxidation of Ni–Cr alloys leads to complex oxide scales comprising Ni(Cr)O solid solutions, $NiCr_2O_4$ spinel, and Cr_2O_3 corundum within the NiO matrix. Understanding the atomic-scale mechanisms of Cr segregation and precipitate formation is crucial for enhancing oxidation resistance. Here, we employ density functional theory calculations to investigate Cr behavior on NiO(100), (110), and (111) surfaces and in the bulk. Our results reveal that isolated Cr atoms preferentially segregate to the surfaces, stabilizing Ni(Cr)O solid solutions *via* strong Cr–O bonding, whereas Cr pairs and clusters favor subsurface migration and bulk aggregation, promoting nucleation of $NiCr_2O_4$ and Cr_2O_3 phases. These findings elucidate a size-dependent segregation mechanism linking Cr coordination environments to oxide phase evolution. This atomic-scale insight informs strategies to tailor oxide microstructures and enhance the high-temperature oxidation resistance of Ni–Cr alloys.

1. Introduction

Ni-based alloys are metallic systems in which Ni serves as the primary constituent, alloyed with other metals such as Fe, Cr, and Al[1–4] to optimize performance. Owing to their exceptional mechanical and chemical properties, these alloys are widely used across a range of industrial applications. For instance, Ni-based alloys possess excellent high-temperature strength, fatigue resistance, and long-term durability, making them ideal for aerospace applications such as turbine blades, combustion chambers, and other critical jet engine components exposed to intense thermal and mechanical stresses.[5,6] Additionally, their outstanding corrosion resistance also positions them well-suited for use in chemical processing equipment, including reactors, storage tanks, pipes, and pipelines, where resistance to aggressive media like acids and alkalis is paramount.[7,8] Beyond aerospace and chemical sectors, Ni-based alloys also play a pivotal role in advanced energy technologies. Their exceptional ability to retain structural integrity under extreme temperatures, intense radiation, and highly corrosive environments makes them indispensable in the energy sector, particularly for nuclear reactors, where they are widely used in components such as fuel cladding and nuclear fuel assemblies.[9,10]

Among various Ni-based alloys, Ni–Cr alloys stand out for their exceptional oxidation and corrosion resistance, largely due to the high oxygen affinity of Cr. During oxidation, Cr is preferentially oxidized to form a protective Cr_2O_3 layer, which acts as a barrier, significantly slowing further degradation of the alloy.[11,12] However, the oxidation behavior of Ni–Cr alloys depends on the temperature, exposure duration, and alloy composition, often resulting in complex, multilayered oxide structures.[13–17]

For example, Calvarin *et al.*[18] examined the oxidation behavior of the Ni–20 wt% Cr alloy in O_2 at 600 °C and 900 °C for durations of 10 min and 48 h. At 600 °C, a 10 min exposure produced a bilayer oxide scale: an outer NiO layer and an inner layer containing both NiO and Cr_2O_3 particles. After 48 h, the oxide scale evolved into three zones: an outer NiO layer, an intermediate layer of NiO, Cr_2O_3, and $NiCr_2O_4$, and an internal oxidation zone with rod-like Cr_2O_3 structures extending towards the substrate. At 900 °C, a 10 min exposure resulted in an outer NiO layer and an inner layer dominated by $NiCr_2O_4$ with Cr_2O_3 precipitates. After 48 h, the oxide structure comprised an outer NiO layer, a middle $NiCr_2O_4$ layer and an internal oxidation zone featuring a continuous Cr_2O_3 layer. The study attributed differences in the internal oxidation zone to temperature-dependent Cr ion diffusion, which, when insufficient at lower temperatures, inhibited the formation of a continuous Cr_2O_3 layer and allowed deeper oxygen penetration.

Liu *et al.*[19] investigated the effect of Cr content on long-term oxidation at 900 °C for over 100 h, using Ni–Cr alloys with Cr

---

[a] *School of Materials Science and Engineering, Xiangtan University, Xiangtan, 411105, China. E-mail: cycai@xtu.edu.cn*
[b] *Key Laboratory of Low Dimensional Materials & Application Technology of Ministry of Education, Xiangtan University, Xiangtan, 411105, China*
[c] *Changjun High School of Changsha City, Changsha, 410013, China*
[d] *Yuhua Institute of Advanced Materials, Baoji Xigong Titanium Alloy Products Co., Ltd, Baoji, 721300, China. E-mail: liuyujing@iamyuhua.com*
[e] *Department of Mechanical Engineering & Materials Science and Engineering Program, State University of New York, Binghamton, NY, 13902, USA. E-mail: gzhou@binghamton.edu*

contents ranging from 9 to 45 wt%. For the 9 wt% Cr alloy, the oxide scale included a NiO outer layer, a porous inner layer of NiO and $NiCr_2O_4$, and an internal oxidation zone with dispersed rod- or round-shaped Cr_2O_3 particles. This porous structure significantly impaired oxidation resistance. Alloys with 18–36 wt% Cr primarily formed a continuous Cr_2O_3 film, effectively suppressing the growth of NiO and $NiCr_2O_4$ and exhibiting superior oxidation resistance. However, the 45 wt% Cr alloy, despite forming a continuous Cr_2O_3 layer, displayed a dual-phase FCC/BCC microstructure prior to the formation of the protective Cr_2O_3 layer. This structure feature led to short-circuit oxidation paths and compromised corrosion resistance.

Nguyen *et al.*[15] further examined the long-term oxidation behavior of NiCr alloys with varying Cr contents by exposing Ni–(5, 10, 20, 25, and 30 wt%)Cr alloys to O_2 at 700 °C for 500 h. Their findings revealed that alloys with lower Cr contents (5, 10, and 20 wt%) developed a two-layer oxide structure: an outer layer of NiO and an inner layer composed of mixed oxides, $(Ni, Cr)_xO$. In contrast, alloys containing 25 and 30 wt% Cr formed a single-layer oxide consisting predominantly of continuous Cr_2O_3. The authors attributed these differences to the availability of Cr during oxidation, which plays a key role in determining the oxide composition and structure.

Existing studies suggest that Ni–Cr alloys with Cr contents up to ∼20 wt% tend to form a two-layer oxide scale during high-temperature oxidation, with the outer layer primarily composed of NiO and the inner layer comprising complex oxide phases such as Ni(Cr)O, $NiCr_2O_4$, and Cr_2O_3. However, the atomic-scale mechanisms governing the nucleation and growth of these precipitate phases during oxidation remain poorly understood. Experimental analysis of these processes at the atomic level is inherently difficult, but first-principles calculations based on density functional theory (DFT) offer a viable approach to address this knowledge gap.

Several previous studies have utilized DFT to explore the formation of oxide precipitates resulting from atomic segregation. For example, Wang *et al.*[20] conducted DFT calculations to investigate the formation of HfO_2 precipitates during high-temperature oxidation of Hf-doped NiAl alloys. Their results indicated that at the γ-Al_2O_3/NiAl interface, the presence of Al vacancy clusters attracted Hf atoms to the interface oxygen, leading to segregation and subsequent HfO_2 formation. Conversely, at the θ-Al_2O_3/NiAl interface, a single Al vacancy within the θ-Al_2O_3 lattice drove Hf atoms into the oxide, similarly resulting in HfO_2 precipitation. Liu *et al.*[21] employed DFT calculations to identify the driving forces behind Al_2O_3 formation in NiCrAl alloys during oxidation. They demonstrated that Al atoms diffused from the NiCrAl substrate into Cr_2O_3, where they preferentially localized at the Ni(111)/Cr_2O_3(0001) interface. Once Al fully replaced Cr at the interface, strong Al–O interactions promoted the formation of Al_2O_3. In another study, Jiang *et al.*[22] examined Pt segregation on various γ-Ni_3Al surfaces ((100), (110), and (111)), showing that Pt atoms preferentially segregate to the surface, enhancing the oxidation resistance of γ-Ni_3Al.

These findings highlight the strength of DFT in elucidating atomistic mechanisms that are challenging to access experimentally. In the present work, we employ first-principles DFT calculations to investigate the segregation behavior of Cr atoms on the NiO surface and within the NiO bulk. Our approach includes systematic comparisons of Cr doping sites, comprehensive energetic analyses, nudged elastic band (NEB) calculations, charge density and Bader charge analyses, and the Crystal Orbital Hamilton Population (COHP) studies, along with the structural characterization of oxide phases resulting from Cr segregation in the NiO lattice. This study aims to provide a fundamental understanding of the behavior of Cr atoms during high-temperature oxidation of Ni–Cr alloys with a Cr content below 20 wt%. The insights gained are crucial for elucidating the mechanisms underlying the formation of complex oxide phases for guiding the design of Ni–Cr alloys with improved oxidation resistance.

2. Computational details

First-principles methods based on DFT are employed to calculate the formation energies of Cr doping at various sites in the NiO bulk and on the NiO(100), (110), and (111) surfaces. The pristine NiO bulk is modeled as a 2 × 2 × 4 supercell, as illustrated in Fig. 1(a). The surface models of NiO(100), (110), and (111) are constructed with 2 × 4 supercells, with the thicknesses of 6, 8, and 10 atomic layers, respectively. A vacuum slab of 15 Å is added perpendicular to the surface to eliminate spurious interactions between periodic images. For geometry optimizations, all atoms in the bulk model are allowed to relax. For NiO(100), the bottom two layers are fixed, whereas for NiO(110) and NiO(111), the bottom three layers remain fixed.

All calculations are performed using the Vienna *ab initio* simulation package (VASP),[23,24] with the Perdew–Burke–Ernzerhof (PBE) exchange–correlation functional.[25–27] The plane-wave energy cutoff is set to 500 eV. Convergence criteria are set to 10^{-4} eV for total energy and 0.05 eV $Å^{-1}$ for atomic forces. The Brillouin zone is sampled using the Monkhorst–Pack *k*-point grids of 3 × 3 × 3 for the bulk and 3 × 3 × 1 for the surface models, following rigorous convergence tests.

To accurately describe the localized nature of 3d electrons in Ni and Cr atoms, the orbital-dependent Coulomb interaction (Hubbard *U*) and exchange parameter *J* are included using the DFT+*U* formalism. The effective *U*–*J* values used in the calculations are 5.3 eV for Ni 3d electrons and 5.0 eV for Cr 3d electrons.[28,29] NiO crystallizes in the rock-salt structure with the space group of $Fm\bar{3}m$. The fully relaxed lattice parameter obtained from DFT calculations is 4.16 Å, in excellent agreement with the experimental value of ∼4.17 Å.[30] To simulate Cr diffusion toward the surface, we construct an initial reaction pathway comprising four intermediate images generated *via* linear interpolation between the fully relaxed initial and final states. The pathway is optimized using the Climbing Image Nudged Elastic Band (CI-NEB) method,[31] and the highest-energy image is identified as the transition state. In the nudged elastic band (NEB) calculations, the diffusion of Cr is modeled *via* a vacancy-assisted mechanism. All calculations, including

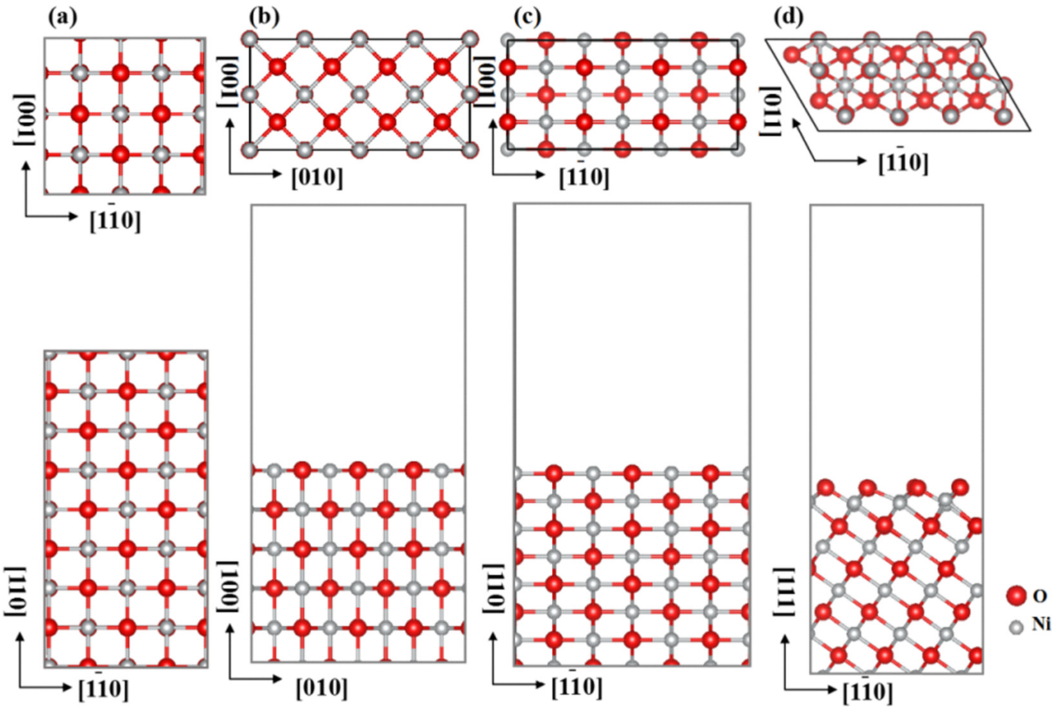

Fig. 1 Structure models used for DFT calculations. (a)–(d): top (upper) and side (lower) views of the NiO bulk and the (100), (110), and (111) surface slabs, respectively. These models form the basis for evaluating Cr doping and segregation in both bulk and surface environments.

the transition-state searches, are performed with spin polarization taken into account.

To provide a quantitative assessment of the Cr–O bonding, the COHP between the Cr atom and its nearest-neighbor O atoms is calculated using the LOBSTER program.[32] This analysis allows a direct comparison of bond strengths across different configurations. To evaluate the site preference of Cr in NiO, the defect formation energy is introduced as a metric, calculated using the following equation:

$$E_{\text{form}} = E_{\text{V}} - E_{\text{perfect}} + \sum_{i} n_i \mu_i \tag{1}$$

where E_{form} is the formation energy of the Cr defect, E_{V} denotes the total energy of the system with a Cr atom substituting a Ni atom, E_{perfect} is the total energy of the pristine NiO system, μ_i represents the chemical potentials of the elements involved (Ni, Cr and O atoms in their standard states), n_i is the number of atoms added ($n_{\text{i}} > 0$) or removed ($n_{\text{i}} < 0$). Specifically, under O-poor conditions, the chemical potentials of Ni and Cr atoms are referenced to their most stable bulk phases (FCC Ni: -5.78 eV; BCC Cr: -9.63 eV),[29] while the O chemical potential is derived from the bulk NiO equilibrium conditions using the following relationship:

$$\mu_{\text{O}} = \frac{1}{N_{\text{O}}}\left[E_{\text{NiO}} - N_{\text{Ni}}\mu_{\text{Ni}}\right] \tag{2}$$

where E_{NiO} represents the standard-state chemical potential of NiO, approximated by the DFT-calculated total energy of the bulk NiO; N_{Ni} and N_{O} denote the numbers of Ni and O atoms in the NiO bulk; and μ_{Ni} is the chemical potential of metallic Ni it its standard state, taken here as -5.78 eV.

Under O-rich conditions, the O chemical potential is referenced to half of the total energy of an O_2 molecule at 0 K relative to the vacuum level (-4.46 eV),[31] and the Ni and Cr chemical potentials are determined from equilibrium with their respective oxides (NiO and Cr_2O_3) using the following relationship:

$$\mu_{\text{M}} = \frac{1}{N_{\text{M}}}\left[E_{\text{MO}} - N_{\text{O}}\mu_{\text{O}}\right] \tag{3}$$

where E_{MO} represents the standard-state chemical potential of the corresponding metal oxide, approximated by the DFT-calculated total energy of its bulk crystal; N_{M} and N_{O} denote the numbers of metal and O atoms in the bulk oxide; μ_{O} is the O chemical potential, taken here as -4.46 eV. The surface energy (γ^{0}_{surf}) is determined using the following equation:

$$\gamma^{0}_{\text{surf}} = \frac{\left[E_{\text{slab}} - mE_{\text{bulk}}\right]}{2A} \tag{4}$$

where E_{slab} and E_{bulk} represent the total energies of the slab and the bulk NiO, respectively; and m is the number of atoms in the slab and A is the surface area.

3. Results

3.1 Cr segregation sites in bulk NiO and on its surfaces

To quantitatively assess the thermodynamic driving force for Cr segregation and the nucleation of Cr-rich oxide phases, we perform a chemical-potential-based formation energy analysis under both O-poor and O-rich conditions. Formation energies

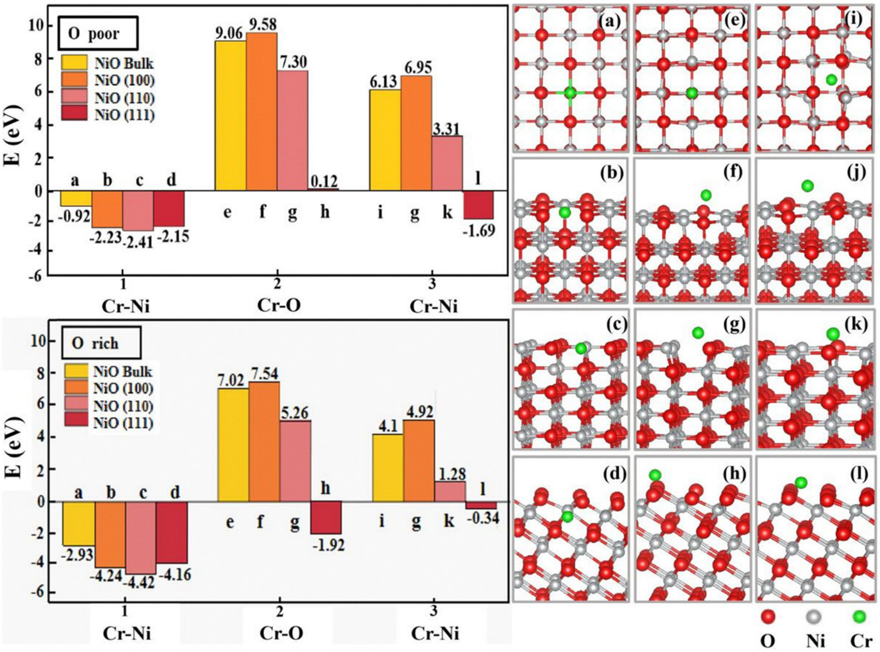

Fig. 2 Formation energies of Cr in the NiO bulk and on NiO surfaces. The left panels show calculated formation energies for Cr occupying different lattice sites, and the corresponding atomic models are shown on the right. Configurations include Cr substitution at Ni sites in the (a) NiO bulk, (b) NiO(100), (c) NiO(110), and (d) NiO(111); Cr substitution at O sites in the (e) NiO bulk, (f) NiO(100), (g) NiO(110), and (h) NiO(111); and Cr incorporation at interstitial sites in the (i) NiO bulk, (j) NiO(100), (k) NiO(110), and (l) NiO(111).

are calculated for Cr occupying crystallographically distinct sites, including Ni substitutional sites, O substitutional sites, and interstitial sites in the NiO bulk and on the NiO(100), (110), and (111) surfaces (Fig. 2). The results show that, under both O-poor and O-rich conditions, Cr substitution at Ni sites consistently exhibits the lowest formation energies, ranging from −0.92 to −4.42 eV, depending on surface orientation and oxygen chemical potential. In contrast, Cr incorporation at O sites or interstitial positions is energetically unfavorable, with formation energies exceeding 1–9 eV. These results quantitatively establish substitutional Cr at Ni sites as the thermodynamically preferred configuration; accordingly, all subsequent calculations consider Cr only in this configuration.

The analysis further reveals that O-rich conditions substantially reduce Cr formation energies by up to ∼2 eV relative to O-poor conditions, indicating that increasing oxygen chemical potential strongly enhances Cr incorporation and stabilization within NiO. This provides a clear thermodynamic basis for the Cr enrichment and aggregation under oxidizing environments. As Cr concentration increases, the combined effects of lowered formation energies, strengthened Cr–O bonding, and higher coordination environments favor Cr–Cr association and inward migration, thereby reducing the free-energy cost of nucleating $NiCr_2O_4$ spinel and Cr_2O_3 corundum phases within the NiO matrix.

3.2 Surface properties

Lower surface energy corresponds to higher surface stability. As shown in Table 1, the stability of the three surfaces follows the order: NiO(100) > NiO(110) > NiO(111)–O > NiO(111)–Ni.

Table 1 Calculated surface energies of NiO(100), NiO(110), and NiO(111) surfaces

Surface	γ^0_{surf} (J m^{-2})
(100)	0.592
(110)	1.794
O-(111)	3.584
Ni-(111)	3.859

To further substantiate the relative stability of the NiO(111) surface terminations, we compare the partial density of states (PDOS) for O-terminated and Ni-terminated surfaces (Fig. S1). The O-terminated surface exhibits a reduced density of states near the Fermi level and stronger hybridization between the O 2p and Ni 3d states, indicative of enhanced Ni–O bonding and improved electronic stability. In contrast, the Ni-terminated surface shows pronounced Ni-derived states near the Fermi level, reflecting undercoordinated surface Ni atoms that are energetically unfavorable under oxidizing conditions. These electronic-structure characteristics provide direct evidence for the greater thermodynamic stability of the O-terminated NiO(111) surface, consistent with previous studies demonstrating that oxygen-terminated oxide surfaces are favored in oxidizing environments.[33,34] Therefore, only the O-terminated NiO(111) is considered in the following Cr segregation analysis.

3.3 Cr segregation on NiO(100)

Fig. 3(a) presents the calculated formation energies for a single Cr atom occupying different surface and subsurface sites of NiO (100). The results show that the formation energies for Cr at the

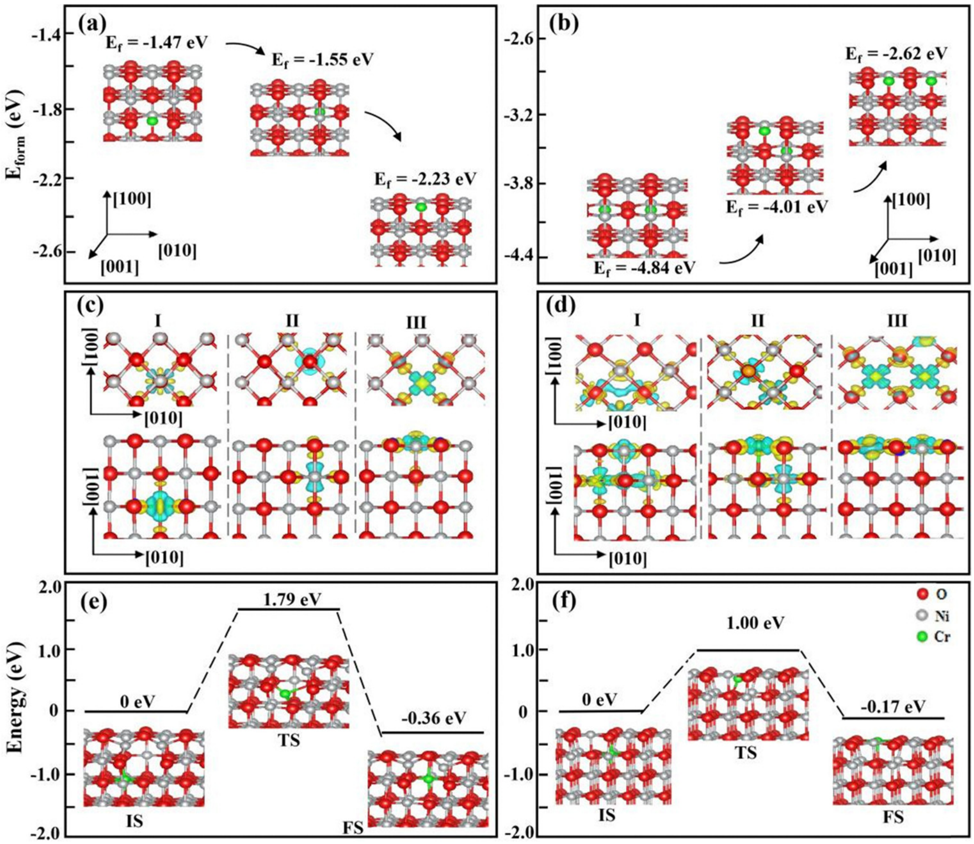

Fig. 3 Structural and electronic characteristics of Cr segregation at various sites of NiO(100). (a) Structural models and the corresponding formation energies of a single Cr atom segregated at the third, second, and surface layers, respectively; (b) structural models and formation energies for two Cr atoms segregated at the second layer, one Cr atom at the surface and the other at the second layer, and both Cr atoms at the surface; (c) differential charge density maps (top and front views) corresponding to the configurations in (a), illustrating electron redistribution around segregated Cr atoms and neighboring O atoms; (d) differential charge density maps (top and front views) corresponding to the configurations in (b). Yellow regions indicate electron accumulation, while blue regions represent electron depletion. (e) and (f) Diffusion paths and energy profiles of a Cr atom on NiO(100).

third layer (approximating the NiO bulk lattice), second layer, and surface are −1.47 eV, −1.55 eV, and −2.23 eV, respectively. These values indicate that Cr can stably occur in all three sites, with the surface site being the most energetically favorable for segregation. To further analyze Cr segregation behavior, Fig. 3(b) shows the system energies for configurations involving two Cr atoms: both located in the subsurface, one in the subsurface and one on the surface, and both on the surface. The corresponding formation energies are −4.84 eV, −4.01 eV, and −2.62 eV, respectively. These results suggest that while Cr segregation to the surface is energetically favorable, configurations where both Cr atoms occupy the subsurface or bulk-like positions are more stable. This implies a thermodynamic preference for Cr atoms to migrate from the surface into the NiO bulk.

To investigate the microscopic mechanism underlying Cr segregation on the NiO(100) surface, we performed charge density difference analysis for Cr atoms and their neighboring O atoms based on the configurations shown in Fig. 3(a) and (b). The results are illustrated in Fig. 3(c) and (d), where the yellow and blue regions represent electron accumulation and depletion, respectively. By comparing the charge density difference for a single Cr atom in the third layer [Fig. 3(c-I)] and the second layer [Fig. 3(c-II)], it is evident that the in-plane Cr–O interactions are similar in both cases. However, the Cr atom in the second layer exhibits stronger interactions with O atoms in the adjacent upper and lower layers, suggesting enhanced bonding stability compared to the third-layer subsurface site. When a single Cr atom segregates to the NiO(100) surface [Fig. 3(c-III)], the strongest charge accumulation occurs between the Cr atom and both the underlying O atom and in-pane O atoms. This pronounced interaction indicates that surface segregation is the most energetically favorable configuration for a single Cr atom.

To visualize the spatial charge distribution variations between Cr atoms and neighboring O atoms, the charge density differences of these atoms are calculated. Fig. 3(c) and (d) present the charge density difference analysis for three configurations involving two Cr atoms: (i) both Cr atoms segregating to the NiO(100) subsurface (the second layer), (ii) one Cr atom segregating to the second layer while the other to the surface layer, and (iii) both Cr atoms segregating to the surface layer. A comparison between Fig. 3(d-III) and (d-II) reveals that the electron accumulation (yellow regions) around in-plane

O atoms is nearly identical for both the surface and subsurface Cr atoms, suggesting comparable Cr–O interactions with the same atomic layer. However, the surface-segregated Cr atoms exhibit minimal interaction with O atoms in adjacent layers, whereas the subsurface Cr atoms display significant interactions with O atoms located directly above and below. This vertical bonding contributes to greater structural stability in the configuration where one Cr atom occupies the surface and the other the subsurface, relative to the case where both reside at the surface. In Fig. 3(d-I), where both Cr atoms are segregated to the NiO(100) subsurface, a prominent blue (electron-deficient) region appears between the Cr atoms, while strong yellow (electron-rich) regions emerge around the neighboring O atoms in the same plan. Additionally, O atoms in the vertical direction—especially those directly beneath the Cr atoms—also show significant electron accumulation. These features indicate stronger Cr–O interactions in multiple directions, enhancing system stability. Thus, the configuration with both Cr atoms in the subsurface is the most thermodynamically favorable among the three scenarios.

NEB calculations are performed to examine the diffusion of a Cr atom on the NiO(100) surface. As shown in Fig. 3(e), diffusion from the sub-subsurface to the subsurface layer through a Ni vacancy site yields an energy barrier of 1.79 eV. In contrast, diffusion from the subsurface to the surface layer through the same pathway has a substantially lower barrier of 1.00 eV (Fig. 3(f)). These results reveal a clear trend: the diffusion barrier decreases progressively as the Cr atom migrates toward the surface, indicating an increasing thermodynamic and kinetic driving force for surface segregation.

The above results demonstrate that the segregation behavior and mechanisms of Cr atoms are highly consistent across the three representative NiO surfaces. To further elucidate the underlying bonding characteristics, COHP analysis is performed for these surfaces. Fig. 4(a–c) show the COHP diagrams between Cr atoms and their nearest neighboring O atoms when a single Cr atom segregates to the sub-subsurface, subsurface, and surface sites of NiO(100), respectively. In the energy range of 0 to −8 eV, the Cr–O anti-bonding states at the surface are notably weaker (*i.e.*, higher in energy and less favorable for bonding). Conversely, within the −21 to −18 eV range, the contribution of Cr–O bonding states (stabilizing interactions) is substantially greater for surface sites compared to subsurface and sub-subsurface positions. The integrated COHP (−ICOHP) values, which quantify the overall bonding strength, follow the order: $\mathrm{Cr}_{\text{1st-layer}}$ (−3.08) > $\mathrm{Cr}_{\text{2nd-layer}}$ (−2.48) > $\mathrm{Cr}_{\text{3rd-layer}}$ (−2.41), indicating stronger Cr–O bonding at the surface.

Fig. 4(d–f) present the COHP diagrams for configurations involving two segregated Cr atoms on NiO(100): both in the sub-surface sites, one in subsurface and one on the surface, and both on the surface. In the 0 to −8 eV range, the Cr–O bonding contributions are significantly enhanced when both the Cr atoms occupy subsurface sites compared to the other configurations. Meanwhile, in the −21 to −18 eV range, surface Cr–O bonds also contribute appreciably to structural stabilization. The corresponding −ICOHP values indicate the following bond strength hierarchy: $\mathrm{Cr}_{\text{2nd-layer}}/\mathrm{Cr}_{\text{2nd-layer}}$ (−3.02) > $\mathrm{Cr}_{\text{1st-layer}}/\mathrm{Cr}_{\text{2nd-layer}}$ (−2.42) > $\mathrm{Cr}_{\text{1st-layer}}/\mathrm{Cr}_{\text{1st-layer}}$ (−2.02).

Table 2 summarizes the Bader charges of Cr atoms segregating on the NiO(100) surface and their adjacent O atoms. In the case of a single Cr atom, the Bader charge increases from 1.282*e* in the bulk to 1.331*e* at the surface, indicating enhanced localization of the electron density around the Cr atoms. Additionally, the average Bader charge of the surface O atoms interacting with subsurface Cr is −1.224*e*, slightly less negative than the −1.233*e* value for O atoms interacting with surface Cr. This suggests that the single surface Cr atom experiences

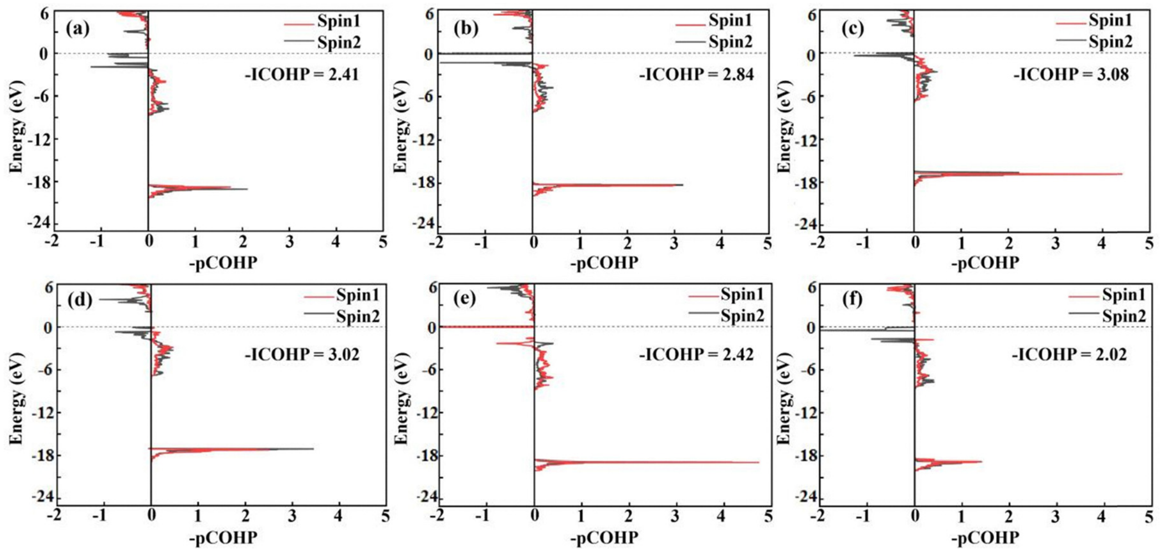

Fig. 4 COHP diagrams of Cr–O bonding interactions. (a)–(c) COHP diagrams for a single Cr atom segregated at the sub-subsurface, subsurface, and surface sites of NiO(100), respectively. (d)–(f) COHP diagrams for two Cr atoms at different segregation configurations of NiO(100): (d) both in subsurface sites, (e) one in the subsurface and one on the surface, and (f) both on the surface.

Table 2 Bader charge analysis of Cr atoms and their neighboring O atoms on the NiO(100) surface. Positive values indicate electron loss, while negative values indicate electron gain. For each configuration, Bader charges of O atoms in the same layer are averaged to represent overall charge redistribution around the Cr segregation sites

Cr position	Cr	In-plane O	Upper-layer O	Lower-layer O
$Cr_{1st\text{-}layer}$	1.331	−1.233		−1.206
$Cr_{2nd\text{-}layer}$	1.290	−1.209	−1.224	−1.191
$Cr_{3rd\text{-}layer}$	1.282	−1.200	−1.185	−1.182
$Cr_{1st\text{-}layer}/Cr_{1st\text{-}layer}$	1.332/1.330	−1.242		−1.170
$Cr_{1st\text{-}layer}/Cr_{2nd\text{-}layer}$	1.340/1.345	−1.224/−1.240		−1.209
$Cr_{2nd\text{-}layer}/Cr_{2nd\text{-}layer}$	1.453/1.454	−1.268	−1.206	−1.214

stronger attraction to adjacent O atoms. In the case of two Cr atoms, the highest Bader charges are observed when both Cr atoms are located in the subsurface (1.454*e* and 1.453*e*), while the corresponding in-plane O atoms exhibit the lowest average Bader charge of −1.268*e*. The results reveal significantly enhanced electron density localization at subsurface Cr sites, correlating with strengthened orbital interactions with adjacent O atoms, reinforcing the conclusion that Cr segregation into the subsurface is energetically and electronically more favorable.

3.4 Cr segregation on NiO(110)

Fig. 5(a) shows the structural models and corresponding system energies for a single Cr atom occupying various subsurface and surface sites of NiO(110). The calculated defect formation energies for Cr segregation to the third layer (considered part of the bulk), second layer, and surface are −2.02 eV, −2.23 eV, and −2.41 eV, respectively. These results indicate that Cr atoms can stably exist at all three sites, with the surface site being the most energetically favorable for single Cr atom segregation on NiO(110). To explore the interaction between multiple Cr atoms, we further compute the system energies for three configurations: (i) both Cr atoms segregated to the second layer, (ii) one Cr atom at the surface and the other in the second layer, and both Cr atoms on the surface, as shown in Fig. 5(b). The corresponding defect formation energies are −4.61 eV, −4.52 eV, and −4.36 eV, respectively. These values indicate that two Cr atoms are energetically favorable whether they reside on the surface or within the bulk. However, the lowest energy configuration occurs when both Cr atoms segregate into the subsurface, implying a preference for Cr incorporation into the subsurface and bulk rather than accumulation on the outermost surface.

To better understand the atomic-scale mechanism underlying this segregation behavior, we perform charge density differential analysis for the Cr atoms and their neighboring O atoms, as shown in Fig. 5(c) and (d). For a single Cr atom located in the third layer [Fig. 5(c-I)], the charge redistribution around neighboring O atoms is minimal, indicating weak interaction and relatively low stabilization in this configuration. In contrast, when Cr occupies the second layer [Fig. 5(c-II)], the interaction between the Cr atom and the O atoms directly above and below becomes significantly stronger—especially with the O atom directly above—suggesting improved stability compared to the third layer case. When the Cr atom is located at the NiO(110) surface [Fig. 5(c-III)], pronounced electron accumulation is observed, especially in the form of ring-like yellow regions on the in-plane O atoms closest to Cr. This indicates stronger bonding interactions between Cr and surrounding O atoms, making the surface site the most stable for single Cr atom segregation on the NiO(110) facet. Overall, these energetic and electronic structure analyses demonstrate that Cr atoms exhibit a strong preference for the NiO(100) surface site due to enhanced Cr–O interactions.

However, when multiple Cr atoms are involved, subsurface and bulk segregation become more favorable, due to collective stabilization effects. Fig. 5(d) shows the differential charge density distributions for three configurations: both Cr atoms are in the subsurface layer [Fig. 5(d-I)], one Cr atom is located at the surface and the other in the subsurface [Fig. 5(d-II)], and both Cr atoms are segregated to the NiO(110) surface [Fig. 5(d-III)]. The charge density distribution for the configuration where both Cr atoms are segregated to the subsurface [Fig. 5(d-I)] shows a significant blue electron depletion zone between the Cr atoms, indicating a region of electron redistribution. Surrounding this region, pronounced yellow electron accumulation is observed on neighboring O atoms. Notably, the O atoms above and below the Cr atoms—particularly those in the lower atomic plane—exhibit strong electron enrichment. This redistribution pattern implies intensified Cr–O bonding and more efficient charge transfer in this configuration. In Fig. 5(d-III), the in-plane O atoms around the Cr atoms display ring-shaped yellow regions, indicating localized electron accumulation. Additionally, the O atoms located in the second layer also show electron enrichment, suggesting moderate Cr–O interactions. Fig. 5(d-II) reveals a similar pattern of electron accumulation around the O atoms adjacent to the surface Cr atom. However, the electron density near the subsurface Cr atom exhibits more pronounced electron accumulation, especially between the two Cr atoms, where the O atoms enhanced electron gains. This suggests stronger Cr–O interactions in the subsurface region compared to the surface. Together, these observations indicate that while Cr atoms can stably segregate to both the surface and subsurface of NiO(110), the dual subsurface configuration promotes stronger Cr–O interactions and offers greater energetic stabilization due to enhanced charge localization and bonding strength.

Fig. 5(e) and (f) present NEB-calculated diffusion pathways for a single Cr atom on the NiO(110) surface. Diffusion from the sub-subsurface to the subsurface *via* a Ni vacancy site yields an energy barrier of 1.59 eV (Fig. 5(e)), whereas further diffusion from the subsurface to the surface layer proceeds with a lower barrier of 1.24 eV (Fig. 5(f)). These results clearly indicate a systematic reduction in the diffusion barrier as the Cr atom approaches the surface, highlighting an increasing kinetic driving force for surface-directed migration.

Fig. 6(a–c) show the COHP diagrams between a single Cr atom and its nearest-neighbor O atoms as the Cr atom segregates to the sub-subsurface, subsurface, and surface sites of

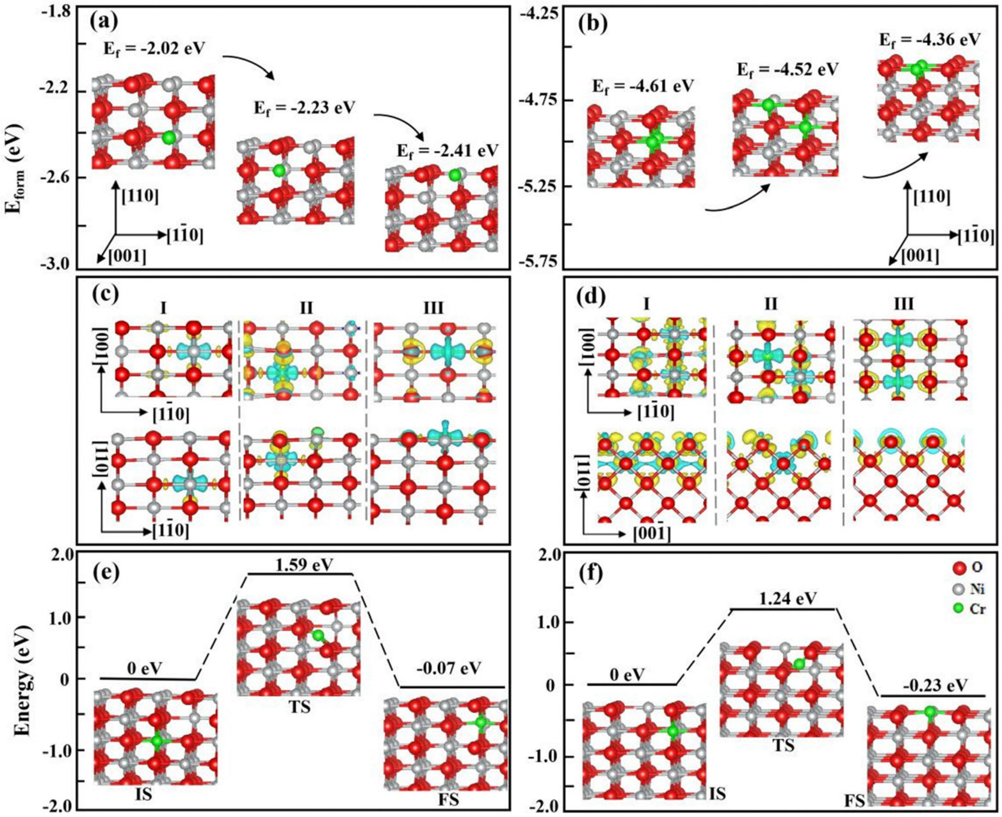

Fig. 5 Structural and electronic characteristics of Cr segregation at various sites of NiO(110). (a) Structural models and the corresponding defect formation energies for a single Cr atom located in the third, second, and surface layers. (b) Formation energies for configurations involving two Cr atoms: both in the second layer, one in the second layer and one at the surface, and both at the surface. (c) Differential charge density maps (top and front views) for the single Cr configurations in (a). (d) Differential charge density maps (top and side views) for dual Cr configurations in (b). Yellow and blue regions indicate electron accumulation and depletion, respectively. (e) and (f) Diffusion paths and energy profiles of a Cr atom on NiO(110).

NiO(110), respectively. The analysis reveals that in the energy range from 0 to −8 eV, the Cr–O antibonding states at the surface are weaker (*i.e.*, higher in energy and thus less favorable for bonding). In contrast, within the −21 and −18 eV range, the contribution of Cr–O bonding states—which stabilize the structure by lowering the total energy—is markedly enhanced at the surface compared to the subsurface and sub-subsurface sites. Correspondingly, the calculated −ICOHP values become progressively more negative from the bulk toward the surface: $Cr_{1st\text{-}layer}$ (−3.89) > $Cr_{2nd\text{-}layer}$ (−3.42) > $Cr_{3rd\text{-}layer}$ (−3.29), confirming that the Cr–O bond strength increases as the Cr atom moves closer to the surface.

Fig. 6(d–f) present the COHP diagrams for configurations involving two Cr atoms segregating to the NiO(110) surface: (d) both in subsurface sites, (e) one in the subsurface and one on the surface, and (f) both on the surface. In the 0 to −8 eV range, the strongest Cr–O bonding contributions are observed when both Cr atoms occupy subsurface sites, while additional surface-related bonding contributions appear between −21 and −18 eV. The overall bond strength, as reflected by the −ICOHP values, follows the trend of $Cr_{2nd\text{-}layer}/Cr_{2nd\text{-}layer}$ (−3.84) > $Cr_{1st\text{-}layer}/Cr_{2nd\text{-}layer}$ (−3.52) > $Cr_{1st\text{-}layer}/Cr_{1st\text{-}layer}$ (−3.40), indicating enhanced stability for subsurface-segregated Cr configurations.

Table 3 summarizes the Bader charges of Cr atoms and their adjacent O atoms of the NiO(110). For single Cr atom segregation: as the Cr atom moves from the bulk (the third layer) to the surface, its Bader charge increases from 1.322*e* to 1.625*e*, indicating enhanced localization of the electron density around the Cr atoms. Notably, the average Bader charge of O atoms interacting with the second-layer Cr atom is −1.233*e*, slightly lower than that (−1.245*e*) of O atoms interacting with the surface Cr atoms. This trend suggests that the surface O atoms more strongly attract Cr, promoting Cr segregation toward the surface. For dual Cr atom segregation: the highest Bader charges are observed for Cr atoms located in the third layer (1.647*e* and 1.637*e*), while the average Bader charge of the surrounding in-plane O atoms is the lowest (−1.250*e*). This indicates that when both Cr atoms occupy third-layer positions, the enhanced Cr–O interactions contribute to improved energy stability.

3.5 Cr segregation on NiO(111)

Fig. 7(a) presents the calculated formation energies for a single Cr atom occupying various surface and subsurface sites of NiO(111). The results show that the formation energies for Cr located at the third Ni layer (approximating the NiO bulk lattice), the second Ni layer, and the surface Ni layer are −1.38 eV, −1.44 eV, and −2.15 eV, respectively. These values

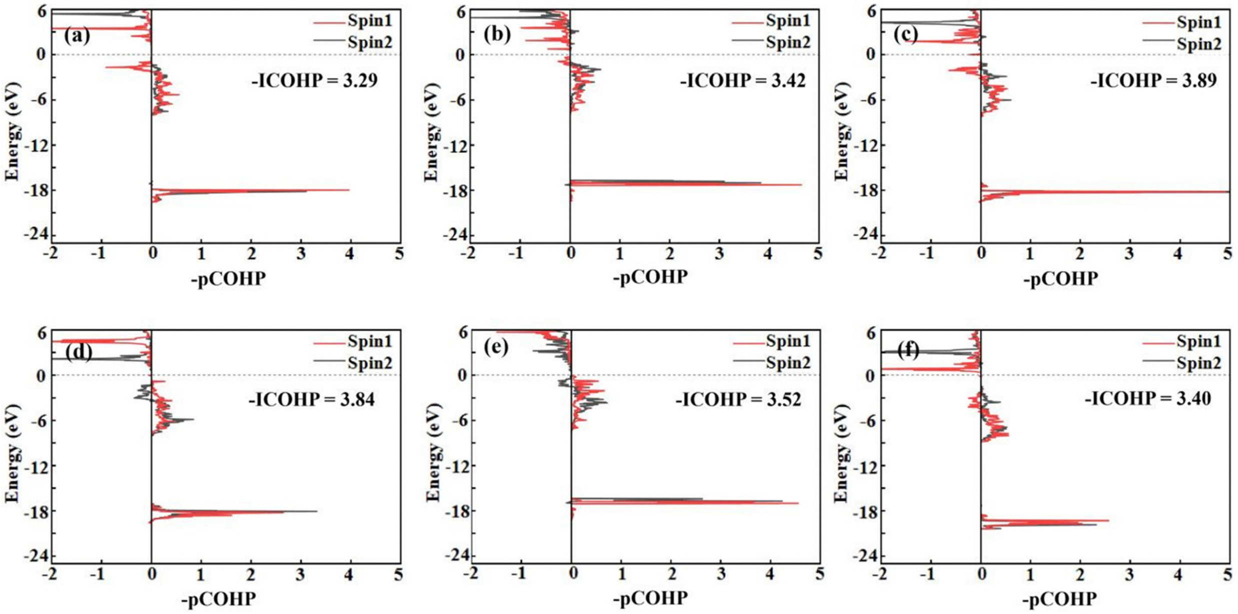

Fig. 6 COHP diagrams of Cr–O bonding interactions. (a)–(c) COHP diagrams for a single Cr atom segregated at different sites (sub-subsurface, subsurface, and surface) of NiO(110). (d)–(f) COHP diagrams for two Cr atoms at different segregation configurations of NiO(110): (d) both in subsurface sites, (e) one in the subsurface and one on the surface, and (f) both on the surface.

Table 3 Bader charge analysis of Cr atoms and their neighboring O atoms on the NiO(110) surface. Positive values indicate electron loss, while negative values indicate electron gain. For each configuration, Bader charges of O atoms in the same layer are averaged to represent overall charge redistribution around the Cr segregation sites

Cr position	Cr	In-plane O	Upper-layer O	Lower-layer O
$\mathrm{Cr}_{\text{1st-layer}}$	1.625	−1.245		−1.215
$\mathrm{Cr}_{\text{2nd-layer}}$	1.467	−1.233	−1.188	−1.170
$\mathrm{Cr}_{\text{3rd-layer}}$	1.322	−1.084	−1.190	−1.188
$\mathrm{Cr}_{\text{1st-layer}}/\mathrm{Cr}_{\text{1st-layer}}$	1.299/1.299	−1.190		−1.156
$\mathrm{Cr}_{\text{1st-layere}}/\mathrm{Cr}_{\text{2nd-layer}}$	1.266/1.616	−1.121/−1.176		−1.187
$\mathrm{Cr}_{\text{2nd-layer}}/\mathrm{Cr}_{\text{2nd-layer}}$	1.647/1.637	−1.212	−1.102	−1.250

indicate that Cr can be stably accommodated at all three sites, with segregation to the surface Ni layer being the most energetically favorable. To further explore Cr segregation behavior, Fig. 7(b) shows the system energies for three configurations involving two Cr atoms: (i) both Cr atoms segregating to the second Ni layer, (ii) one Cr atom segregating to the second Ni layer while the other at the surface, and (iii) both Cr atoms segregating to the surface. The corresponding formation energies are −6.05 eV, −4.93 eV, and −4.53 eV, respectively. These results indicate that, although surface segregation is energetically favorable for a single Cr atom, the configurations with both Cr atoms in the subsurface (or bulk-like) positions is more stable overall. This suggests a thermodynamic tendency for Cr atoms to accumulate in the NiO bulk.

To investigate the microscopic mechanism underlying Cr segregation, we performed charge density difference analysis for Cr atoms and their neighboring O atoms, based on the configurations shown in Fig. 7(a) and (b). On the NiO(111) surface, there are no O atoms in the same atomic layer as Cr; thus, charge transfer occurs between Cr and the adjacent O atoms located above and below, as shown in Fig. 7(c) and (d). Comparative analysis of the charge density differences for a single Cr atom located in the third Ni layer (bulk-like), second Ni layer (subsurface), and surface Ni layer (shown in Fig. 7(c-I), (c-II), and (c-III), respectively) reveals distinct electron accumulation (yellow regions) around neighboring O atoms. In all cases, Cr atoms show charge transfer toward adjacent O atoms, with more significant electron accumulation on the upper O atoms—particularly for Cr in the surface Ni layer. Notably, the Cr atom at the surface exhibits the most pronounced charge transfer to nearby O atoms, as indicated by the expanded yellow regions. This stronger Cr–O interaction suggests that segregation of a single Cr atom to the surface Ni layer is energetically more favorable, consistent with the formation energy trends.

In the configuration where both Cr atoms are located in the second Ni layer [Fig. 7(d-I)], a cloud-like blue region appears between the two Cr atoms, indicating electron depletion. Simultaneously, more pronounced yellow electron accumulation is observed in adjacent O layers, highlighting stronger Cr–O interactions deeper within the NiO lattice. In Fig. 7(d-II), one Cr atom resides in the second Ni layer and the other in the surface Ni layer. Here, prominent electron accumulation is seen particularly around the O atoms in the second layer, suggesting enhanced Cr–O interactions extending from the surface through to the third O layer. Fig. 7(d-III) illustrates the case where both Cr atoms occupy the surface Ni layer of NiO(111). Yellow regions of electron density accumulation are observed around the adjacent O atoms, indicating attractive interactions between the Cr atoms and O atoms in the surface and second

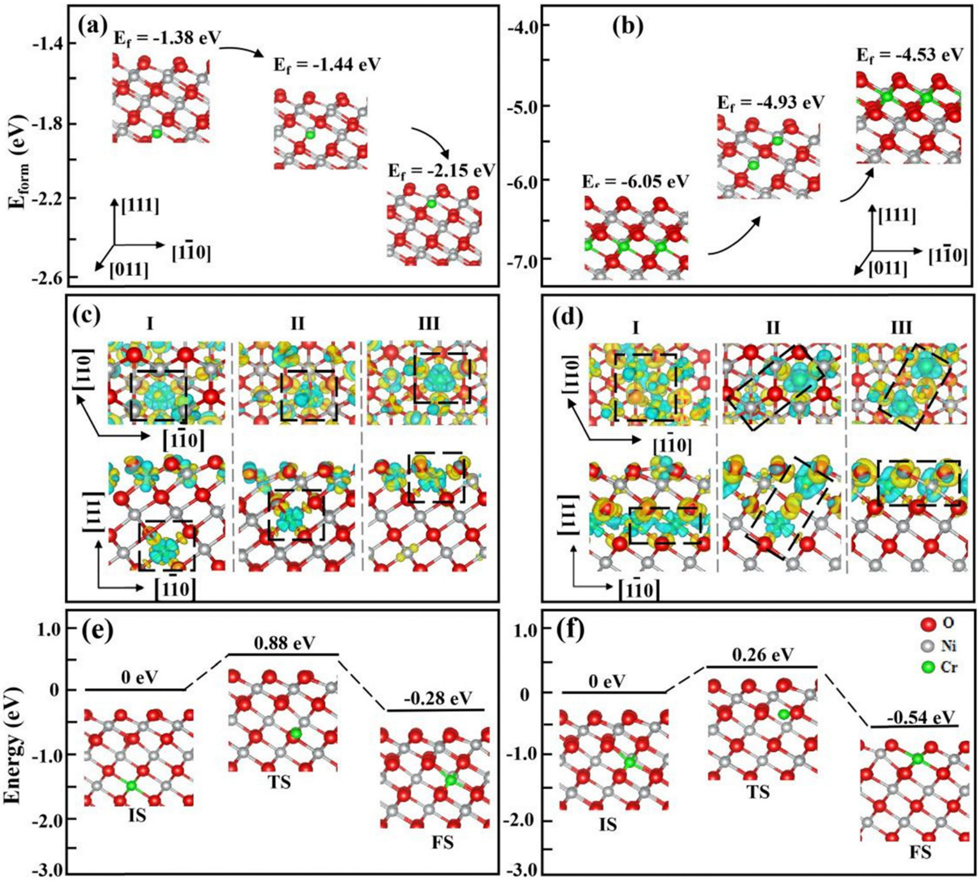

Fig. 7 Structural and electronic characteristics of Cr segregation at various sites of NiO(111). (a) Structural models and the corresponding defect formation energies for a single Cr atom located in the third, second, and surface Ni layers. (b) Formation energies for configurations involving two Cr atoms: both in the second Ni layer, one in the second Ni layer and one at the surface, and both at the surface. (c) Differential charge density maps (top and front views) for the single Cr configurations in (a). (d) Differential charge density maps (top and front views) for dual Cr configurations in (b). Yellow and blue regions indicate electron accumulation and depletion, respectively. (e) and (f) Diffusion paths and energy profiles of a Cr atom on NiO(111).

O layers. These charge redistribution patterns suggest that the configuration with both Cr atoms in the second Ni layer is the most energetically stable.

Fig. 7(e) and (f) show NEB-calculated diffusion pathways for a single Cr atom on the NiO(111) surface. Diffusion from the third Ni layer to the second Ni layer *via* a Ni vacancy site exhibits an energy barrier of 0.88 eV (Fig. 7(e)). Subsequent migration from the second Ni layer to the surface Ni layer proceeds with a much lower barrier of 0.26 eV (Fig. 7(f)). These results demonstrate a progressive decrease in the diffusion barrier as the Cr atom moves closer to the surface.

Fig. 8(a–c) present COHP diagrams between the Cr atom and its nearest-neighbor O atoms as single Cr atom segregates to the sub-subsurface, subsurface, and surface sites of NiO(111), respectively. The analysis shows that within the energy range from 0 to −8 eV, the Cr–O antibonding states at the surface are weaker. In contrast, in the range of −21 to −18 eV, the contribution from Cr–O bonding states—which lower the system energy and stabilize the structure—is significantly greater at the surface than at the subsurface or sub-subsurface sites. Consistent with these observations, the −ICOHP values become more negative in the order $Cr_{1st\text{-}Ni\text{-}layer}$ (−3.75) > $Cr_{2nd\text{-}Ni\text{-}layer}$ (−3.49) > $Cr_{3rd\text{-}Ni\text{-}layer}$ (−3.06), confirming that the Cr–O bond strength increases as the Cr atom moves toward the surface.

Fig. 8(d–f) display the corresponding COHP diagrams for two Cr atoms segregating to the NiO(111) surface in different configurations: both in subsurface sites, one in the subsurface and one on the surface, and both on the surface. The results indicate that within the 0 to −8 eV range, the Cr–O bonding states contribute most significantly when both Cr atoms reside in subsurface sites. Additional bonding contributions are also observed in the −21 and −18 eV range for surface Cr–O interactions. The overall bond strength, as quantified by the −ICOHP values, follows the order $Cr_{2nd\text{-}Ni\text{-}layer}/Cr_{2nd\text{-}Ni\text{-}layer}$ (−3.99) > $Cr_{1st\text{-}Ni\text{-}layer}/Cr_{2nd\text{-}Ni\text{-}layer}$ (−3.08) > $Cr_{1st\text{-}Ni\text{-}layer}/Cr_{1st\text{-}Ni\text{-}layer}$ (−2.66), indicating that subsurface configurations are the most energetically favorable for Cr–O bonding.

Table 4 summarizes the Bader charges of Cr atoms and their neighboring O atoms of NiO(111). For single Cr atom segregation, the Bader charge increases from 1.661*e* in the third Ni layer (bulk-like) to 1.680*e* in the surface Ni layer, indicating enhanced localization of the electron density around the Cr atoms. Notably, the average Bader charge of the O atoms interacting with Cr in the second-Ni layer is −1.196*e*, slightly

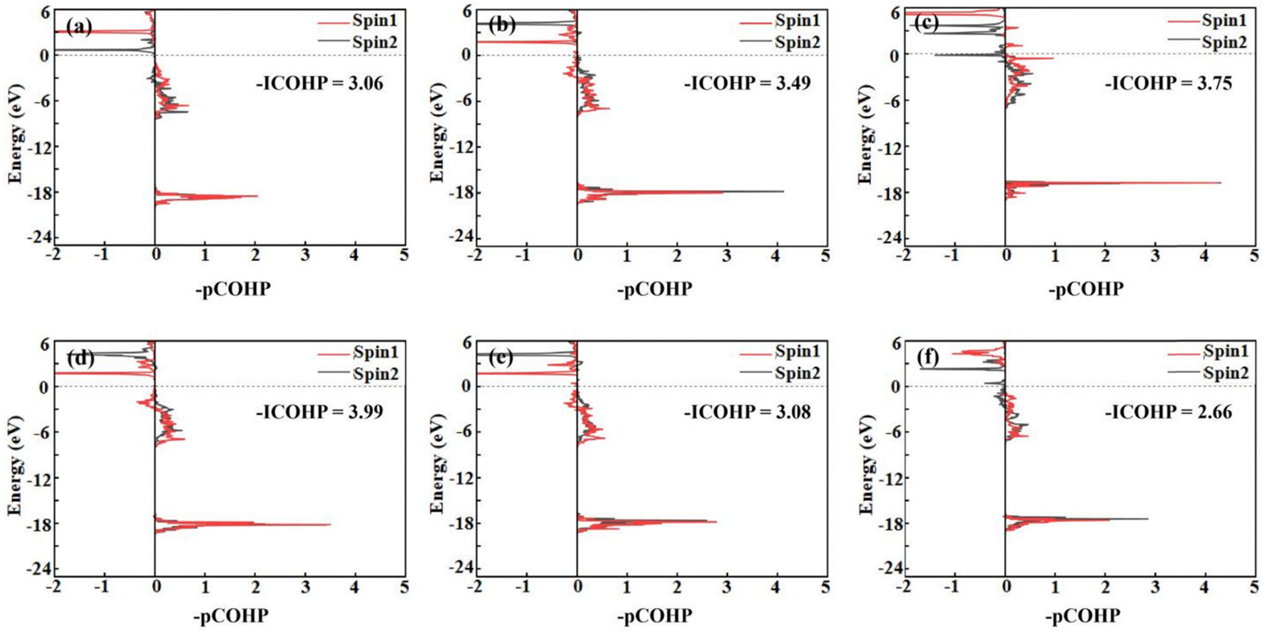

Fig. 8 COHP diagrams of Cr–O bonds. (a)–(c) COHP diagrams for a single Cr atom segregated at different sites (sub-subsurface, subsurface, and surface) of NiO(111). (d)–(f) COHP diagrams for two Cr atoms at different segregation configurations of NiO(111): (d) both in subsurface sites, (e) one in the subsurface and one on the surface, and (f) both on the surface.

Table 4 Bader charge analysis of Cr atoms and their neighboring O atoms in NiO(111). Positive values indicate electron loss, while negative values indicate electron gain. For each configuration, the Bader charges of O atoms within the same layer are averaged to represent the overall charge redistribution around the Cr segregation sites

Cr position	Cr	In-plane O	Upper-layer O	Lower-layer O
$Cr_{1st\text{-}Ni\ layer}$	1.680		−1.250	−1.150
$Cr_{2nd\text{-}Ni\ layer}$	1.674		−1.196	−1.189
$Cr_{3rd\text{-}Ni\ layer}$	1.661		−1.198	−1.154
		$O_{1st\text{-}O\ layer}$	$O_{2nd\text{-}O\ layer}$	$O_{3rd\text{-}O\ layer}$
$Cr_{1st\text{-}Ni\ layer}/Cr_{1st\text{-}Ni\ layer}$	1.652/1.659	−0.854	−1.172	
$Cr_{1st\text{-}Ni\ layer}/Cr_{2nd\text{-}Ni\ layer}$	1.674/1.772	−0.833	−1.203	−1.161
$Cr_{2nd\text{-}Ni\ layer}/Cr_{2nd\text{-}Ni\ layer}$	1.775/1.754		−1.235	−1.202

lower than that for O atoms (−1.250*e*) adjacent to surface-segregated Cr, reflecting stronger electrostatic attraction between Cr and surface O atoms. This supports the trend of Cr segregation toward the surface. For configurations with two Cr atoms, the case where both occupy the second Ni layer shows the highest Bader charges (1.775*e* and 1.754*e*) for Cr and the lowest average Bader charge for surrounding O atoms (−1.235*e*). These results confirm that Cr atoms in the second Ni layer exhibit strong electron localization and form stronger interactions with neighboring O atoms, contributing to the energetic stability of this configuration.

3.6 Cr segregation in the NiO bulk

The computational results above indicate that in the presence of multiple Cr atoms, segregation into the NiO bulk is energetically favorable. To further explore this behavior, we investigate Cr segregation within a NiO bulk model. Fig. 9(a) and (b) present the total formation energies of systems containing two and three Cr atoms, respectively, in both dispersed and aggregated configurations within the bulk lattice. For two Cr atoms, the formation energies are calculated as −0.90 eV for the dispersed configuration and −1.14 eV for the aggregated configuration. Similarly, for three Cr atoms, the formation energies are −1.70 eV (dispersed) and −2.23 eV (aggregated). In both cases, Cr aggregation is energetically preferred, with aggregation energies being lower by 0.24 eV and 0.53 eV, respectively, compared to the dispersed counterparts. These results suggest a clear thermodynamic tendency for Cr atoms to cluster within the NiO bulk. Moreover, the comparison between the aggregation energies of two and three Cr atoms shows that the formation energy becomes significantly more favorable (by 1.09 eV) when a third Cr atom is introduced. This trend indicates that higher Cr concentrations promote aggregation, which likely drives the formation of complex oxide phases during high-temperature oxidation.

To further elucidate the driving forces behind Cr atom aggregation and dispersion in the NiO bulk, differential charge density analyses were performed on the configurations shown in Fig. 9(a) and (b), with the results presented in Fig. 9(c) and (d). In the case of two Cr atoms dispersed within the NiO bulk [Fig. 9(c-I)], small blue regions representing electron depletion are observed on the Cr atoms, while only minor yellow regions—indicative of electron accumulation—appear on the neighboring O atoms. This suggests weak interactions between Cr and surrounding O atoms in the dispersed state. In contrast, when the two Cr atoms aggregate [Fig. 9(c-II)], a large, continuous blue

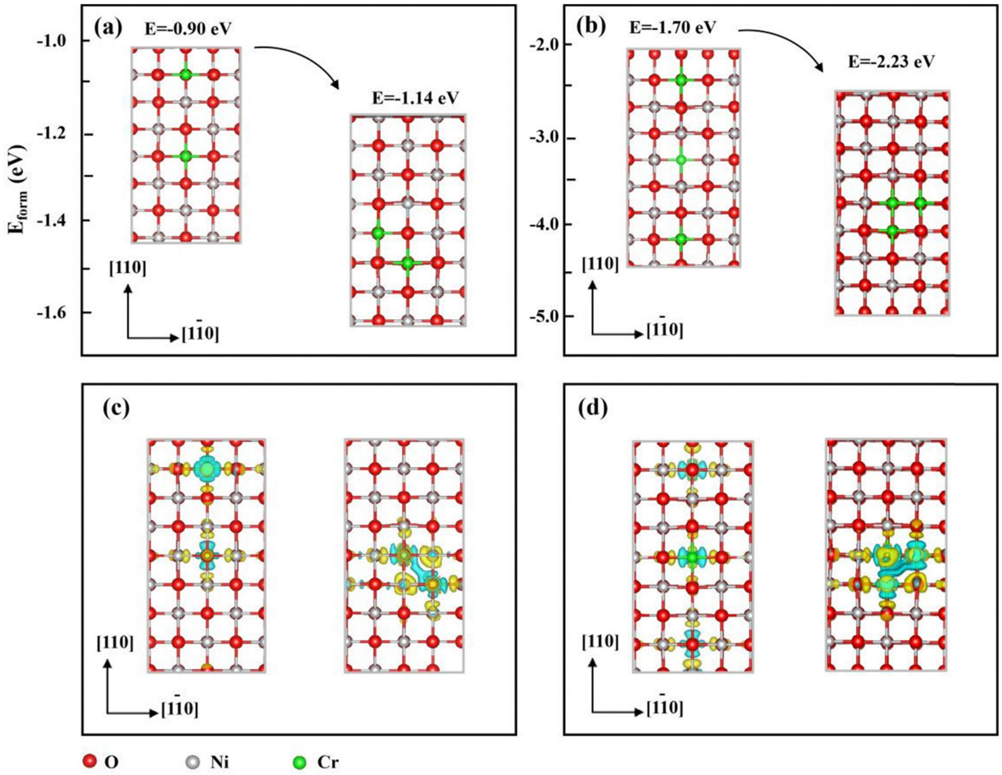

Fig. 9 Cr segregation behavior charge redistribution in the NiO(100) bulk. (a) Structural models and the corresponding formation energies for two Cr atoms in dispersed and aggregated configurations in NiO; (b) structural models and the corresponding formation energies for three Cr atoms in dispersed and aggregated configurations in NiO; (c) differential charge density maps (front view) corresponding to the configurations in (a), illustrating electron redistribution around segregated Cr atoms and neighboring O atoms; (d) differential charge density maps (front view) corresponding to the configurations in (b). Yellow regions indicate electron accumulation, while blue regions represent electron depletion.

electron depletion region emerges between them, accompanied by more prominent yellow electron accumulation regions on adjacent O atoms. This pattern reflects significantly enhanced Cr–O interactions, which energetically favor aggregation. A similar trend is observed for systems with three Cr atoms. In the dispersed configuration [Fig. 9(d-I)], weak Cr–O interactions are indicated by limited charge redistribution—small blue regions on Cr atoms and minor yellow regions on neighboring O atoms. However, when the three Cr atoms aggregate [Fig. 9(d-II)], a more extensive blue electron depletion region forms among the Cr atoms, along with intensified yellow electron accumulation around surrounding O atoms. Notably, the depletion region among three Cr atoms is even more pronounced than that observed for two Cr atoms, highlighting that Cr–O interactions strengthen with increasing Cr concentration. These findings confirm that Cr aggregation in the NiO bulk is driven by enhanced charge transfer and stronger Cr–O bonding interactions, especially at higher Cr concentrations.

Table 5 summarizes the Bader charges of Cr atoms and their neighboring O atoms of NiO bulk. For two Cr atoms in NiO, the Bader charges of Cr are 1.338*e* (aggregated) and 1.292*e* (dispersed), while the corresponding O atoms exhibit charges of −1.121*e* and −1.109*e*, respectively. In the case of three Cr atoms, the aggregated configuration yields average Cr charges of 1.422*e*, compared to 1.282*e* for the dispersed case, with O atoms averaging −1.157*e* and −1.089*e*, respectively. Notably, Cr aggregation increases the average Bader charges of Cr by 0.046*e* (two Cr) and 0.140*e* (three Cr), while the neighboring O atoms show increases of 0.012*e* and 0.068*e*, respectively. This demonstrates enhanced charge transfer between Cr and O atoms when Cr clusters form in the NiO bulk. Furthermore, comparing the aggregated configurations, the average Bader charges of Cr and O atoms increase by 0.084*e* and 0.036*e*, respectively, when the Cr count rises from two to three. Cr atoms in the aggregated state show enhanced electron localization and stronger interactions with adjacent O atoms, demonstrating that increasing Cr concentration intensifies charge redistribution and strengthens Cr–O electronic interactions.

Table 5 Bader charge analysis of Cr atoms and their neighboring O atoms in the NiO bulk. Positive values indicate electron loss, while negative values indicate electron gain

Cr position	Cr	O
Two aggregated Cr atoms	1.338	−1.121
Two dispersed Cr atoms	1.292	−1.109
Three aggregated Cr atoms	1.422	−1.157
Three dispersed Cr atoms	1.282	−1.089

Fig. 10(a and b) present COHP diagrams for two Cr atoms in dispersed and aggregated configurations within the NiO bulk.

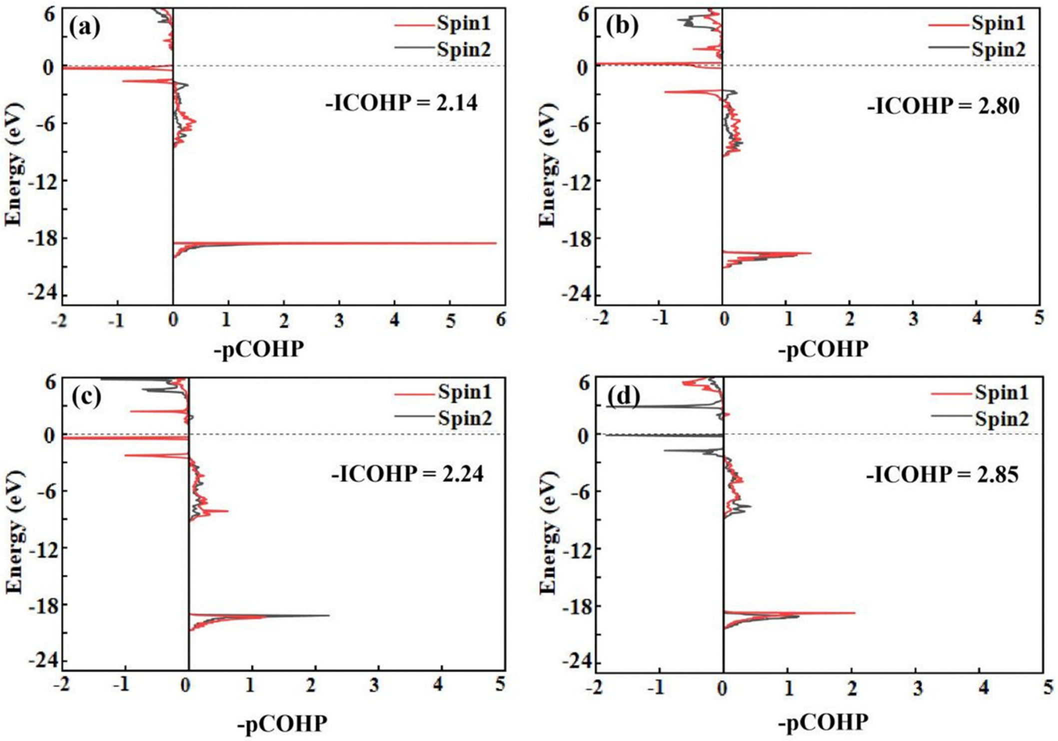

Fig. 10 COHP diagrams for Cr–O bonds in bulk NiO: (a) and (c) dispersed Cr atoms; (b) and (d) aggregated Cr atoms.

The analysis reveals that in the aggregated state, Cr–O bonding states dominate across both the 0 to −8 eV and −21 to −18 eV energy ranges, indicating stronger Cr–O interactions. The corresponding −ICOHP values confirm this trend: Cr-aggregated (−2.80) > Cr-dispersed (−2.14), signifying enhanced bond stability in the aggregated configuration. Similarly, Fig. 10(c and d) show the COHP results for another set of dispersed and aggregated Cr configurations within the NiO bulk, which exhibit a consistent trend with Cr-aggregated (−2.85) > Cr-dispersed (−2.24). These results collectively demonstrate that Cr aggregation strengthens Cr–O bonding and stabilizes the local oxide structure.

4. Discussion

The combined NEB and COHP analyses reveal a size- and environment-dependent mechanism governing Cr segregation, migration, and oxide phase evolution during Ni–Cr oxidation. COHP calculations were performed for a comprehensive set of configurations involving isolated Cr atoms and Cr pairs located at the surface, subsurface, and sub-subsurface sites on NiO(100), (110), and (111) surfaces, as well as in the bulk (Figs. S2–S8). Orbital-resolved COHP analysis shows that the site-dependent electronic structure is primarily controlled by Cr–O hybridization. In the upper valence-band region (0 to −8 eV), the dominant contributions arise from Cr 3d–O 2p interactions. For surface- and near-surface-segregated isolated Cr atoms, the Cr–O antibonding states in this energy range are significantly weakened (shifted to higher energies), indicating reduced antibonding character and enhanced local stability of the Ni(Cr)O solid solution. This redistribution of valence states provides a direct electronic-structure origin for the thermodynamic preference of isolated Cr for surface segregation.

In contrast, when Cr atoms aggregate into pairs or small clusters, cooperative Cr–O bonding effects emerge. In addition to enhanced Cr 3d–O 2p bonding near the valence band, pronounced bonding features appear in deeper energy windows (−21 to −18 eV), dominated by Cr 4p/4s–O 2s hybridization. These deeper bonding states significantly lower the total energy and stabilize higher-coordination Cr–O environments, thermodynamically favoring subsurface migration and bulk aggregation. Such electronic-structure evolution promotes the nucleation of $NiCr_2O_4$ spinel and Cr_2O_3 corundum phases within the NiO matrix. Consistent with this picture, NEB calculations show a systematic decrease in diffusion barriers as an isolated Cr atom approaches the surface, reflecting the same electronic driving force that stabilizes surface-segregated Ni(Cr)O. Together, these results establish an atomic-scale framework linking Cr coordination, orbital-resolved electronic structure, transport kinetics, and oxide phase evolution, providing mechanistic insight into the formation of complex Cr-rich oxide scales in Ni–Cr alloys.

Analysis of the Cr–O bond lengths and bond angles (Fig. 11) shows that aggregated Cr atoms in NiO exhibit bond lengths of 2.07–2.21 Å and bond angles of 87.53°–92.64°. These values are comparable to those reported for $NiCr_2O_4$ (Cr–O: 1.98–2.03 Å; angles: 83.66°–95.78°)[35] and Cr_2O_3 (Cr–O: 1.97–2.04 Å; angles: 79.86°–100.70°),[36] indicating that Cr aggregation within the

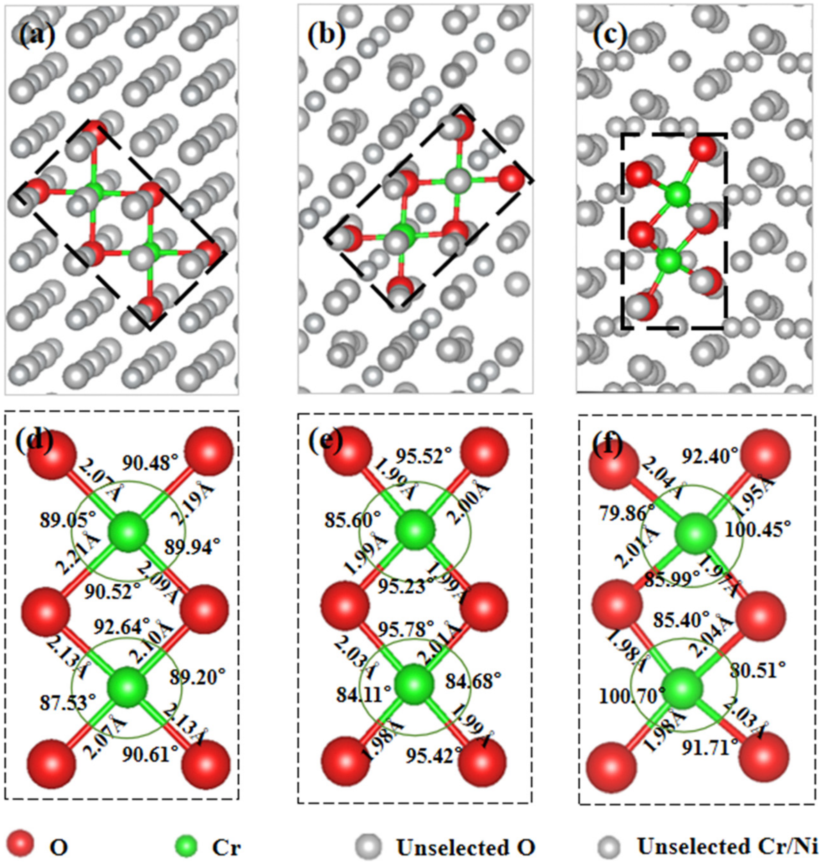

Fig. 11 Comparison of Cr–O local bonding environments. (a) Cr–O bond lengths and bond angles for aggregated Cr atoms embedded in the NiO lattice; (b) Cr–O bond lengths and bond angles in bulk $NiCr_2O_4$; (c) Cr–O bond lengths and bond angles in bulk Cr_2O_3; (d)–(f) Enlarged views of the local Cr–O configuration environments highlighted by the dashed boxes in (a)–(c), respectively, illustrating the structural similarities between aggregated Cr in NiO and the corresponding Cr-rich oxide phases.

NiO bulk locally reproduces coordination environments characteristic of spinel and corundum phases. This structural similarity provides an atomistic link between Cr aggregation and the nucleation of Cr-rich oxide precipitates.

DFT calculations across NiO(100), (110), and (111) surfaces and the bulk reveal a concentration-dependent segregation mechanism. At low Cr concentrations, isolated Cr atoms preferentially segregate to surfaces or interfaces, where they are stabilized by favorable Cr–O bonding and promote the formation of Ni(Cr)O solid solutions. This behavior supports the development of continuous, protective oxide layers during early oxidation. In contrast, increasing Cr concentration shifts the thermodynamic preference toward subsurface and bulk incorporation, where Cr atoms tend to aggregate rather than remain isolated. These aggregated configurations are energetically stabilized by cooperative Cr–O bonding and higher local coordination, driving the emergence of $NiCr_2O_4$ spinel and Cr_2O_3-like structural motifs.

These computational results are consistent with experimental observations showing Ni(Cr)O solid solutions at low Cr contents and the formation of Cr_2O_3 and $NiCr_2O_4$ precipitates at higher Cr loadings during high-temperature oxidation of Ni–Cr alloys.[37] By directly linking atomic-scale Cr segregation and aggregation to macroscopic oxide phase evolution, the simulations establish a unified mechanistic framework for understanding Cr-driven oxide scale development.

The atomistic insights obtained here further suggest clear guidelines for alloy design aimed at enhancing high-temperature oxidation resistance. Oxidation behavior is governed by a balance between isolated Cr stabilization at the NiO surface—which favors continuous Ni(Cr)O solid solutions—and Cr aggregation in subsurface or bulk regions, which promotes the formation of spinel and sesquioxide precipitates. Alloying strategies that suppress Cr–Cr association or reduce Cr mobility can therefore help maintain a high population of surface-segregated Cr, enhancing the stability and integrity of protective oxide scales. For example, elements with strong oxygen affinity, such as Al or Si,[38,39] may compete with Cr for O coordination, weakening cooperative Cr–O bonding and suppressing Cr clustering. Alternatively, refractory elements with low diffusivity (*e.g.*, W, Mo, or Ta[40–43]) may kinetically hinder Cr aggregation by increasing the migration barriers through lattice strain or defect trapping. More broadly, these results indicate that deliberate tuning of Cr–O hybridization and Cr transport kinetics through targeted alloying provides a viable pathway to engineer oxide microstructures that favor stable solid-solution oxides over Cr-rich precipitates, thereby improving oxidation resistance under aggressive service conditions.

5. Conclusions

This study employed density functional theory calculations to systematically investigate the segregation behavior of Cr atoms on NiO (100), (110), and (111) surfaces, as well as their role in oxide phase formation within the NiO bulk. Formation energy calculations reveal that at low concentrations, Cr atoms preferentially segregate to the NiO surfaces across all three orientations. In contrast, at higher concentrations, Cr tends to accumulate in the subsurface and bulk regions. Within the NiO bulk, Cr atoms show a pronounced tendency to aggregate, forming configurations with structural characteristics similar to those of $NiCr_2O_4$ or Cr_2O_3. Differential charge density and Bader charge analyses further elucidate the driving forces behind these behaviors. At low concentrations, strong electrostatic interactions between Cr atoms and surface O atoms favor surface segregation. At higher concentrations, Cr–Cr interactions become more significant, enhancing Cr–O bonding in the bulk and promoting aggregation. As Cr atoms cluster, their interactions with surrounding O atoms intensify, leading to local structures with characteristics similar to those of complex oxide phases. These results provide an atomistic-level understanding of Cr segregation and precipitation during the high-temperature oxidation of Ni–Cr alloys. The findings are consistent with experimental observations of Ni(Cr)O, $NiCr_2O_4$, and Cr_2O_3 formation, and offer valuable insights for optimizing alloy composition and oxidation conditions to enhance the oxidation resistance of Ni–Cr-based materials.

Conflicts of interest

The authors declare that they have no known competing financial interests or personal relationships that could have appeared to influence the work reported in this paper.

Data availability

All data that support the findings of this study are included within the submitted manuscript.

Supplementary information (SI) is available. See DOI: https://doi.org/10.1039/d5cp04239a.

Acknowledgements

This work was supported by the National Natural Scientific Foundation of China (Grant No. 12074326). The work at Binghamton University was supported by the U.S. Department of Energy, Office of Basic Energy Sciences, Division of Materials Sciences and Engineering under Award No. DE-SC0001135.

References

1 J. Li, Y. Peng, J. Zhang, S. Jiang, S. Yin, J. Ding, Y. Wu, J. Wu, X. Chen and X. Xia, *Vacuum*, 2019, **169**, 108938.

2 S. Liu, W. Li, J. Sun, L. Fu, T. Wang, S. Jiang, J. Gong and C. Sun, *Corros. Sci.*, 2020, **171**, 108703.

3 J. Yang, S. Wang, Y. Li and D. Xu, *Corros. Sci.*, 2020, **167**, 108493.

4 X. Zhuang, Y. Tan, X. You, P. Li, L. Zhao, C. Cui, H. Zhang and H. Cui, *Vacuum*, 2021, **189**, 110219.

5 T. Baldridge, G. Poling, E. Foroozmehr, R. Kovacevic, T. Metz, V. Kadekar and M. Gupta, *Opt. Lasers Eng.*, 2013, **51**, 180–184.

6 Y. Zhang, H. Yuan, W. Yan, S. Chen, M. Qiu and B. Liao, *ACS Appl. Mater. Interfaces*, 2021, **13**, 58179–58192.

7 D. Jin, F. Yang, Z. Zou, L. Gu, X. Zhao, F. Guo and P. Xiao, *Surf. Coat. Technol.*, 2016, **287**, 55–60.

8 S. Balaguru and M. Gupta, *J. Mater. Res. Technol.*, 2021, **10**, 1210–1242.

9 P. Sengupta, *J. Nucl. Mater.*, 2011, **411**, 181–184.

10 J. S. Alzahrani, Z. Alrowaili, C. Eke, Z. M. Mahmoud, C. Mutuwong and M. Al-Buriahi, *Radiat. Phys. Chem.*, 2022, **195**, 110090.

11 S. Tsai, A. Huntz and C. Dolin, *Mater. Sci. Eng., A*, 1996, **212**, 6–13.

12 A. Huntz and S. Tsai, *J. Mater. Sci. Lett.*, 1994, **13**, 821–825.

13 L. Luo, M. Su, P. Yan, L. Zou, D. K. Schreiber, D. R. Baer, Z. Zhu, G. Zhou, Y. Wang and S. M. Bruemmer, *Nat. Mater.*, 2018, **17**, 514–518.

14 J. Zurek, D. Young, E. Essuman, M. Hänsel, H. Penkalla, L. Niewolak and W. Quadakkers, *Mater. Sci. Eng., A*, 2008, **477**, 259–270.

15 T. D. Nguyen, Y. Xie, S. Ding, J. Zhang and D. J. Young, *Oxid. Met.*, 2017, **87**, 605–616.

16 G. O. Subramanian, H. J. Lee, S. H. Kim and C. Jang, *Oxid. Met.*, 2018, **89**, 683–697.

17 Y. Xie, T. D. Nguyen, J. Zhang and D. J. Young, *Corros. Sci.*, 2019, **146**, 28–43.

18 G. Calvarin, A. Huntz and R. Molins, *Mater. High Temp.*, 2000, **17**, 257–264.

19 S. Liu, Y. Chen, Z. An, J. Zhao, H. Lu, Y. Jiao, L. Xie, A. Li and X. Han, *Corros. Sci.*, 2023, **224**, 111525.

20 X. Wang, C. Cai and G. Zhou, *Appl. Surf. Sci.*, 2022, **578**, 151917.

21 L. Hui, L. Yuping, Z. Caili, D. Nan, L. Aidong, L. HongFei, D. Hongbiao and H. Peide, *Comput. Mater. Sci.*, 2013, **78**, 116–122.

22 C. Jiang and B. Gleeson, *Acta Mater.*, 2007, **55**, 1641–1647.

23 G. Kresse and J. Furthmüller, *Comput. Mater. Sci.*, 1996, **6**, 15–50.

24 G. Kresse and J. Hafner, *Phys. Rev. B: Condens. Matter Mater. Phys.*, 1993, **47**, 558.

25 G. Kresse and D. Joubert, *Phys. Rev. B: Condens. Matter Mater. Phys.*, 1999, **59**, 1758.

26 J. P. Perdew, K. Burke and M. Ernzerhof, *Phys. Rev. Lett.*, 1996, **77**, 3865.

27 S. L. Dudarev, G. A. Botton, S. Y. Savrasov, C. Humphreys and A. P. Sutton, *Phys. Rev. B: Condens. Matter Mater. Phys.*, 1998, **57**, 1505.

28 W.-B. Zhang and B.-Y. Tang, *J. Chem. Phys.*, 2008, 128.

29 Z. Rak and D. Brenner, *J. Appl. Phys.*, 2018, 123.

30 R. Cairns and E. Ott, *J. Am. Chem. Soc.*, 1933, **55**, 527–533.

31 G. Henkelman and H. Jónsson, *J. Chem. Phys.*, 2000, **113**, 9978–9985.

32 R. Dronskowski and P. E. Bloechl, *J. Phys. Chem.*, 1993, **97**, 8617–8624.

33 A. V. Bakulin, S. S. Kulkov and S. E. Kulkova, *Appl. Surf. Sci.*, 2021, **536**, 147639.

34 Y. Gao, M. Iachella, E. Mattson, A. T. Lucero, J. Kim, M. Djafari Rouhani, Y. Chabal, C. Rossi and A. Esteve, *J. Phys. Chem. C*, 2018, **122**, 17856–17864.

35 M. Ptak, M. Maczka, A. Gągor, A. Pikul, L. Macalik and J. Hanuza, *J. Solid State Chem.*, 2013, **201**, 270–279.

36 F. o Lebreau, M. M. Islam, B. Diawara and P. Marcus, *J. Phys. Chem. C*, 2014, **118**, 18133–18145.

37 S. Xiao, Y. Cai, X. Peng, J. Chen, Y. Liu, C. Cai, X. Liu and G. Zhou, *Corros. Sci.*, 2025, **257**, 113332.

38 J. Chen, Y. Tang, F. Liu, J. Shu, Y. Liu, Z. Dong and Y. Liu, *Metall. Mater. Trans. A*, 2020, **52**, 270–283.

39 Z. Zhang, R. F. Webster and J. Zhang, *Corros. Sci.*, 2024, **232**, 112050.

40 C. A. Barrett, R. V. Miner and D. R. Hull, *Oxid. Met.*, 1983, **20**, 255–278.

41 S.-J. Park, K.-H. Lee, S.-M. Seo, H.-W. Jeong, Y.-S. Yoo and H. Jang, *Rare Met.*, 2020, **39**, 918–927.

42 S.-J. Park, S.-M. Seo, Y.-S. Yoo, H.-W. Jeong and H. Jang, *Materials*, 2019, **12**, 2934.

43 Y. Zhang, Z. Li, Y. Gui, H. Fu and J. Xie, *Int. J. Miner., Metall. Mater.*, 2024, **31**, 351–361.